Using Cramér–Rao Theory Combined With Monte Carlo Simulations for the Optimization of Monolithic Scintillator PET Detectors

D. J. (Jan) van der Laan, Marnix C. Maas, Dennis R. Schaart, Peter Bruyndonckx, Sophie Léonard, and Carel W. E. van Eijk, *Member, IEEE*

***Abstract*—We are investigating the possibility of using monolithic scintillator blocks as detectors for small animal positron emission tomography (PET). These detectors consist of several cm^3 of scintillating material, read out by one or more avalanche photo-diode (APD) arrays. The entry point of an incoming gamma photon is estimated from the distribution of the scintillation light over the APD pixels. To optimize the detector design, the influence of different design parameters is investigated using Geant4 simulations. To make it possible to study the influence of individual design parameters on the intrinsic spatial resolution of the detector, the use of a performance measure is proposed that is independent of the algorithm used to estimate the entry point, namely the Cramér–Rao lower bound on the estimation of the coordinates of a point source of light inside the crystal. To illustrate the use of this method, the influence of optical transport inside the detector is investigated for different detector designs, surface finishes and APD pixel sizes. A comparison with resolutions obtained from simulations involving beams of 511 keV annihilation photons indicates that this approach gives valid results.**

***Index Terms*—Cramér–Rao lower bound, depth-of-interaction, Geant4 Monte Carlo simulations, monolithic scintillator blocks, positron emission tomography (PET).**

I. Introduction

In recent years there has been an increase of interest in small animal positron emission tomography (PET). Small animal PET requires a high spatial resolution and, especially when dynamic studies are to be performed, a high sensitivity [1]. In order to achieve the required resolution, most current designs use arrays of small scintillation crystals coupled to position-sensitive photomultiplier tubes (PMTs). Although in principle the resolution can be increased in this design by decreasing the dimensions of the crystals, much sensitivity is lost because of the dead space between the crystals occupied by reflective material for optical separation. Additional dead space may exist between the detector modules, which may, for example, be dictated by the relatively large size of the position-sensitive photomultiplier tubes. Finally, increasing the length of the crystals in order to increase the sensitivity requires correction for the depth-of-interaction (DOI), since otherwise the resulting parallax error will decrease the resolution outside the center of the scanner.

Manuscript received November 15, 2004; revised December 16, 2005.

D. J. van der Laan, M. C. Maas, D. R. Schaart, and C. W. E. van Eijk are with the Delft University of Technology, 2629 JB Delft, The Netherlands (e-mail: d.j.vanderlaan@tnw.tudelft.nl).

P. Bruyndonckx and S. Léonard are with the Inter-University Institute for High Energies, Vrije Universiteit Brussel, 1050 Brussels, Belgium.

Digital Object Identifier 10.1109/TNS.2006.873710

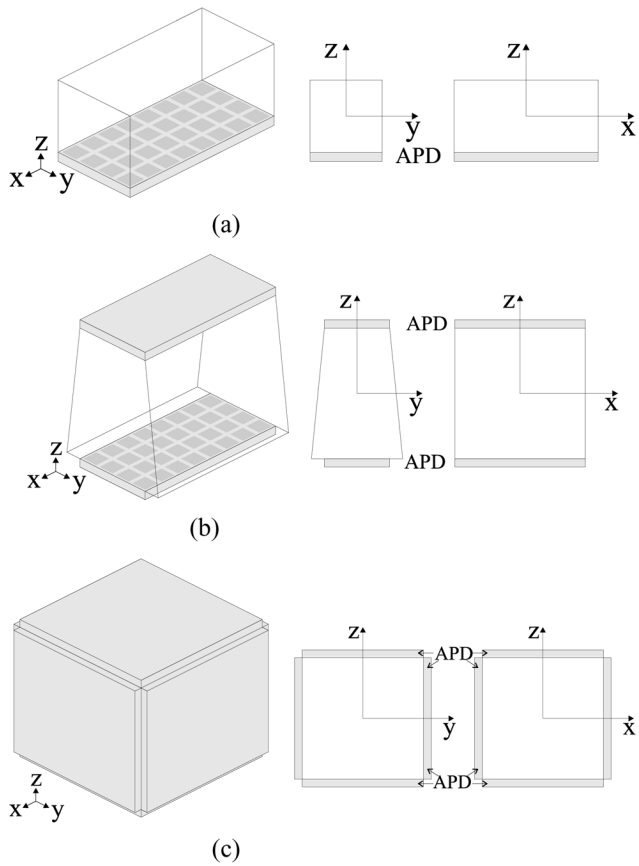

Fig. 1. Three examples of detector design. A $20 \times 10 \times 10$ mm^3 LSO crystal read out on one side by an APD array (a), a 20 mm thick tapered LSO crystal read out by two APD arrays (b), and a $20 \times 20 \times 20$ mm^3 LSO crystal read out on six sides by single APDs (c).

Monolithic scintillation detectors can avoid these problems. These detectors consist of a continuous scintillation crystal read out by position sensitive photo-detectors. The Philips CPET system is, for example, based on this type of detector, although without DOI correction [2]. Designs with DOI correction have also been investigated [3]–[5], but these are either too complicated or have insufficient spatial resolution for small animal PET.

The detectors we are investigating consist of several cubic centimeters of scintillating material coupled on one or more sides to avalanche photo-diode (APD) arrays. Three examples of this detector are shown in Fig. 1. The coordinates of the entry point of an incoming gamma photon are estimated from the light distribution on the pixels of the APD arrays. This can be done

by either a statistical method or neural networks. Before estimation can take place, the algorithm is first trained using measured light distributions produced by annihilation photons with known entry points.

Compared to detectors using arrays of small crystals, the proposed monolithic scintillation detectors have several advantages. First of all, the detection efficiency is increased because the dead space between the crystals in a crystal array is avoided and because the dead space between the detector modules can be minimized due to the small size of the APD arrays. They are also easier to manufacture. Furthermore, integration with MRI devices may become possible because of the use of APD arrays instead of PMTs.

Measurements on this type of detector show that the intrinsic detector resolution is comparable to that of detectors using arrays of small crystals [6]–[8]. However, the resolution obtained in measurements is always determined by a large number of factors, such as the shape of the monolithic scintillator, the crystal surface finish, the width of the beam used in the measurements, electronic noise and the algorithm used to estimate the coordinates of the entry point. This makes it difficult to determine the individual effect of each of these factors on the resolution. Understanding these influences can make optimization of the design more efficient. Monte Carlo simulations mimicking the measurements can help, since certain parameters can be varied more easily in a simulation than in an experiment. Furthermore, influences that are unavoidable in experiments, such as electronic noise, can even be left out completely if one wishes to study solely the effect of other parameters. However, even in such simulations the resolution still depends on the estimation algorithm used. When for example a better spatial resolution is found for a crystal whose surfaces are polished than for an unpolished crystal, it is not known if this is because this specific estimation algorithm works better for crystals with polished surfaces or that the polished crystal is inherently better. Perhaps the detector would perform even better with an unpolished crystal with a different estimation algorithm.

In this paper we propose the use of a performance measure, that is independent of the estimation algorithm, namely the Cramér–Rao lower bound on the estimation of the coordinates of a point source of light inside the crystal. Since this measure gives the lower bound on the variance in the estimated coordinates for any unbiased estimation algorithm, it does not depend on the estimation algorithm used. This makes it possible to better understand the influence of different design parameters on the resolution. After introducing the Cramér–Rao lower bound, we will illustrate it with results obtained from simulations in which the geometry, surface finish and pixel size is varied. Finally, we will compare these results to actual resolutions obtained using a simple estimation algorithm on simulated data.

II. Cramér–Rao Lower Bound

In the monolithic scintillator detectors the entry point of an impinging annihilation photon is estimated from the distribution of the scintillation light over the pixels of the APD arrays using a learning algorithm (for an example see Section III.B) that has been trained using light distributions produced by annihilation photons with known entry points. By estimating the entry point of the annihilation photon the DOI is intrinsically corrected for.

When the annihilation photon deposits its energy in one point inside the crystal, the light distribution is determined by the x, y, and z-coordinate of this interaction point. In that case, the estimation algorithm can be considered to estimate the x, y, and z-coordinate of the interaction point, from which the entry point is calculated using the angle of incidence. In a PET scanner this angle may be derived from the positions of the two detectors firing in coincidence, as is explained in more detail in [8]. In reality, the energy of an annihilation photon will not always be deposited in a single point, due to the occurrence of Compton scattering, X-ray fluorescence, etc. The estimation algorithm will still estimate one entry point, which can be considered to be based on a kind of average interaction point. Even though there may be some blurring in this case, the estimation of entry point can again be considered to be based on the estimation of an interaction point. Therefore, it seems reasonable to assume that the ability to estimate the x, y, and z-coordinates of single point sources of light is a good indicator of the ability to estimate the entry points of realistic events.

For the case of a single point source of light, it is possible to derive the Cramér–Rao lower bound on the estimate of its coordinates. This lower bound equals the smallest value of the standard deviation that any unbiased estimator of the parameters of interest (in this case the coordinates of the point source) can achieve, given a statistical model of the observations (in this case the simulated light distributions). In the following derivation of the statistical model, it is assumed that the annihilation photon deposits all of its energy at position $\underline{x} = (x, y, z)^{\mathrm{T}}$ inside the crystal. The number of optical photons emitted is assumed to follow a Poisson distribution with mean N. N is the light yield of the scintillator at 511 keV.

Assume that P APD pixels detect the optical photons emitted by the point source, and that pixel i detects a fraction $f_i(\underline{x})$ of the optical photons. Then, the number of detected optical photons on a pixel will follow a Poisson distribution and be independent of the number detected on the other pixels. The probability of detecting n_i photons on pixel i is therefore given by

$$p_i(n_i \,|\, \underline{x}, N, \eta) = \frac{(N \cdot \eta \cdot f_i(\underline{x}))^{n_i}}{n_i!} \cdot e^{-N \cdot \eta \cdot f_i(\underline{x})}, \tag{1}$$

where η is the quantum efficiency of the APD array. The likelihood of the pixels detecting $\underline{n} = (n_1, n_2, \ldots, n_P)^{\mathrm{T}}$ photons is given by

$$L(\underline{n} \,|\, \underline{x}, N, \eta) = \prod_{i=1}^{P} p_i(n_i \underline{x}, N, \eta). \tag{2}$$

Using this likelihood function the information matrix is defined as [9]

$$\mathbf{M} = -\mathrm{E}[\partial^2 \ln L(\underline{n} \,|\, \underline{x}, N, \eta)/\partial \underline{x}^2]. \tag{3}$$

The Cramér–Rao inequality, which gives the lower bound on the covariance matrix of an unbiased estimator, then states that

$$\mathrm{cov}(\hat{\underline{x}}, \hat{\underline{x}}) \geq \mathbf{M}^{-1}, \tag{4}$$

where $\hat{\underline{x}}$ is the estimator of the coordinate $\underline{x}$ [9]. The lower bound on the variances on $\hat{x}, \hat{y}$, and $\hat{z}$ are given by the three diagonal elements of this matrix.

Using the likelihood function as defined in (2) and (1), the elements of the information matrix become

$$M_{vw} = N \cdot \eta \cdot \sum_{i=1}^{P} \frac{1}{f_i(\underline{x})} \frac{\partial f_i(\underline{x})}{\partial v} \frac{\partial f_i(\underline{x})}{\partial w}, \tag{5}$$

with v and w equal to x, y, or z. From this equation follows that

$$\mathbf{M}^{-1} \propto \frac{1}{N \cdot \eta}, \tag{6}$$

which shows that the variance is inversely proportional to the number of photons emitted and the quantum efficiency.

To evaluate these expressions for a given point $\underline{x}$ in the crystal, the expectation value of the fraction of photons that reaches each pixel, $f_i(\underline{x})$ and the first derivative of this fraction to each of the coordinates must be known. Both can be estimated using optical Monte Carlo simulations. When a large number of optical photons are tracked through the detector after emission from the point source, the expectation value of the detected fraction can be calculated for each pixel by dividing the number of detected photons by the total number of emitted photons. The partial derivatives of this fraction can be determined by doing the same simulation for points located $\pm h$ in the x, y, and z direction from (x, y, z). The derivative is then found by numerical derivation. For example, the partial derivative to x is estimated by

$$\left.\frac{\partial f_i(x,y,z)}{\partial x}\right|_{x,y,z} = \frac{f_i(x+h,y,z) - f_i(x-h,y,z)}{2h} + O(h^2). \tag{7}$$

The partial derivatives to y and z can be calculated in a similar way.

Although it is in theory possible to derive the lower bound on the estimation of the entry point of an annihilation photon, thus taking Compton scatter and X-ray fluorescence into account, this is not practical. The likelihood has to be derived directly from simulations, since the number of photons detected by the APD pixels will no longer be Poisson distributed and independent. This would take a huge amount of simulation time and would make it necessary to do all calculations numerically thereby loosing the clarity of the method.

The Cramér–Rao theory gives the lower bound on the standard deviation in each of the coordinates. In case of perpendicular incidence of the annihilation photon, only the lower bound on the x and y-coordinate are of importance. However, when the photon has an incident angle, the lower bound on the z-coordinate determines how well the parallax error can be avoided. It appears that the results for the lower bound on the standard deviation of the x-coordinate are often representative for the other coordinates as well, and therefore we will primarily focus on this coordinate. However, when the lower bound on any of the other two coordinates shows interesting behavior, this will of course be discussed.

III. Methods

A. Cramér–Rao Simulations

The Cramér–Rao lower bound has been calculated for a three-dimensional grid of points in a number of different geometries and for several different surface finishes. The simulations needed to calculate the functions $f_i(x, y, z)$ have been performed using the Monte Carlo code Geant4 [10]. With this code it it possible to simulate the transport and interactions of the gamma photons, the scintillation process, and the transport of the optical photons, but for the calculation of the Cramér–Rao lower bound only the transport of optical photons is needed.

In order to reduce computation times, use has been made of symmetry in the detector where possible. For example, all geometries investigated are symmetrical in the x and y-direction. The lower bound therefore needs to be calculated for only one quadrant of the crystal. By mirroring these results the lower bound for the remainder of the crystal is found. For every point source position 1.7 million photons were tracked, and a value of 0.5 mm was chosen for h to calculate the derivative using (7). This value is a compromise between the bias (for large h) and the standard deviation (for small h) in the estimate of the derivative and was determined from preliminary simulations.

Five different geometries have been used in the simulations. In the description of these geometries, the crystal surface facing the center of the scanner is called the front surface.

- A $20 \times 10 \times 10$ mm^3 LSO:Ce_{3+} crystal with a front and back surface of 20 mm $\times$ 10 mm read out on the back side by an APD array. This design is shown in Fig. 1(a).
- A $20 \times 10 \times 20$ mm^3 LSO:Ce_{3+} crystal with a front and back surface of 20 mm $\times$ 10 mm read out on the back and front side by an APD array. The increased thickness of the crystal in this geometry increases the probability of an interaction of an 511 keV annihilation photon from 58% to 83% [11].
- A 20 mm thick tapered LSO:Ce_{3+} crystal, with a 20 mm $\times$ 10 mm front surface and a 20 mm $\times$ 14 mm back surface, see Fig. 1(b). Both surfaces are read out by an APD array. Because of the taper, this shape eliminates almost all dead space between the crystals if they are placed in a ring. The dimensions of this geometry will be written as $20 \times 14(10) \times 20$ mm^3.
- A $20 \times 10 \times 20$ mm^3 $LaBr_3$:Ce_{3+} crystal read out on the back and front side by an APD array. An advantage of $LaBr_3$ is the high light yield (61 000 photons/MeV) compared to LSO (26 000 photons/MeV) [11], since, as follows from (6), the lower bound on the standard deviations is inversely proportional to the square root of the

number of emitted photons per event. However, the density is smaller than that of LSO (5.3 g·cm^{-3} versus 7.4 g·cm^{-3} for LSO) causing the interaction probability of an annihilation photon to be only 61% [11].

- A $20 \times 20 \times 20$ LSO:Ce_{3+} crystal read out on all sides by single-pixel APDs. This design is shown in Fig. 1(c). LeBlanc and Thompson [12] have already reported on simulations on a similar design. The APDs have a surface of 20 mm $\times$ 20 mm. The active area is 16 mm $\times$ 16 mm, which leaves a gap of 2 mm round the edge. The timing and energy resolution could benefit from the fact that almost all light is collected in this design. Since there are no reflections inside the crystal for this design (see the discussion of the optical model below), the Cramér–Rao lower bound can be calculated from the solid angle of the APDs seen from the point source position. The solid angles and the lower bound are therefore calculated numerically for this design.

The model that has been used to simulate the optical interactions at surfaces is the UNIFIED model, which has been described by Levin and Moisan [13]. This model is implemented in Geant4 [14]. In this model a surface consists of small microfacets, whose normals have a random angle, α, with the overall surface normal. The angles follow a normal distribution with an expectation value of zero and a standard deviation of σ_α, which is therefore a measure of surface roughness. In our case, the surface is covered on the outside by a reflective cladding with a refractive index that is equal to that of air. If the cladding is reflective, it reflects the optical photons diffusely.

A number of different surface finishes were investigated. We simulated two types of polished surfaces. One was clad in Teflon (reflectivity 95%) and one in an absorbing material (reflectivity 0%). The same types of cladding were also used for a rough surface. The polished surface was modelled with a σ_α of 0.1° and the rough surface with a σ_α of 6.0°. These values were taken from Moisan *et al.* [15]. As an extreme case we also studied a specularly reflecting surface. The specularly reflecting surface reflects 100% of the optical photons with the angle of reflection equal to the angle of incidence.

In the Cramér–Rao simulations only the refractive indices and the light yield of the scintillating materials are needed. For LSO these are 1.82 and 26 000 photons/MeV respectively and for $LaBr_3$ 1.88 and 61 000 photons/MeV [11], [16]. The optical coupling between the APD arrays and the crystal has been assumed to be perfect. This means that all optical photons reaching the crystal-APD surface are absorbed by the APD array. Furthermore, the quantum efficiency of the APD array has been assumed to be equal to one, since at the moment we are only interested in the effect of the light transport on the resolution. Furthermore, the quantum efficiency has no influence when comparing results from one scintillator to each other, since it is then only a constant factor according to (6).

In our measurements we have been using the Hamamatsu S8550 APD array [6]. The size of the pixels on this array is 1.6 mm $\times$ 1.6 mm and the center to center distance between the pixels is 2.3 mm in both directions. All of the results presented in this paper for the different surface finishes and for the different detector geometries are based on this APD array, except for the $20 \times 20 \times 20$ crystal that is read out by six single APDs. In order to investigate the influence of the APD pixel size on the detector performance, the lower bound for the $20 \times 10 \times 20$ LSO crystal was additionally calculated for four different pixel sizes. Besides the aforementioned pixel size the following sizes were investigated: 1.1 mm $\times$ 1.1 mm with a pitch of 1.8 mm, 3.9 mm $\times$ 1.6 mm with a pitch of 4.6 mm in the x-direction and 2.3 mm in the y-direction, and 3.9 mm $\times$ 3.9 mm with a pitch of 4.6 mm. The numbers of pixels on these arrays are 10×5, 4×4, and 4×2 respectively. In all cases, the pixels are separated by a 0.7 mm dead region.

B. Simulations Using Beams

The results obtained for the Cramér–Rao lower bound were compared to results from simulations that resemble the measurements done in our group [6] and in Brussels [7], [8]. In these simulations a beam of 511 keV gamma photons having a diameter of zero is stepped in steps of 250 μm over the center of the crystal in the x and y-direction. The number of photons detected by each APD pixel was recorded for 400 events for every beam position. Electronic noise was not modeled.

In order to calculate the spatial resolution the entry point of each of the simulated distributions is estimated using the remainder of the distributions as training data for our estimation algorithm. The distribution for which the entry point has to be estimated is compared using least squares to each of the distributions in the training set. The entry point of the distribution in the training set giving the smallest least squares value is used as the estimate of the entry point. The full width at half maximum (FWHM) and the full width at tenth maximum (FWTM) of the histogram of all the errors, defined as the distances between the true and estimated entry points, of the scan are used as a spatial resolution measure. More information on the estimation algorithm and beam measurements has been presented elsewhere [6].

IV. Results and Discussion

A. Cramér–Rao Results

1) Surface Finish: Fig. 2 shows the cumulative distribution of the Cramér–Rao lower bound on the x-coordinate inside the $20 \times 10 \times 20$ mm^3 LSO crystal for the different surface finishes described in the previous section. For example, more than 80% of the crystal volume has a lower bound smaller than 0.4 mm for all surface finishes. The five surface finishes show little performance difference for the lower bound on the x-coordinate. Similar results were obtained for the y-coordinate. The lower bound on the z-coordinate is slightly higher for the specularly reflecting surface than for the other four, more realistic, surface finishes. The surface finish, therefore, seems to have little to no influence on the spatial resolution of the detectors. The polished Teflon clad surface finish is, therefore, used in the comparison of the different detector geometries. This is motivated by the fact that the use of a Teflon wrapped crystal will yield larger and more constant signal amplitudes, which may improve the timing characteristics and the energy resolution of the detector.

2) Crystal Geometry: Figs. 3 and 4(a) show the lower bound on the x-coordinate as a function of position in a plane

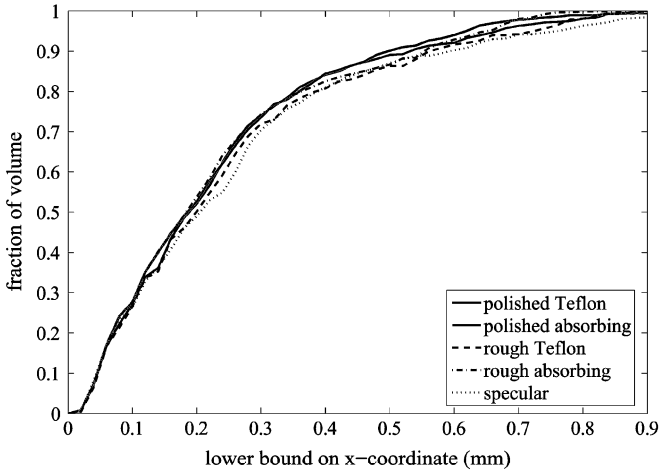

Fig. 2. Cumulative distribution of the Cramér–Rao lower bound on the x-coordinate inside the $20 \times 10 \times 20$ mm^3 LSO crystal for different surface finishes. The y-axis shows the fraction of the crystal volume for which the lower bound is smaller than the value given on the x-axis.

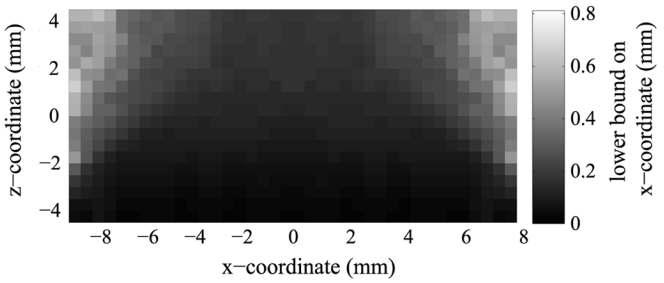

Fig. 3. The lower bound on the x-coordinate as a function of position in the x-z plane in the center of the crystal for the $20 \times 10 \times 10$ mm^3 LSO crystal with polished surfaces and wrapped in Teflon.

in the center of the crystal for the $20 \times 10 \times 10$ mm^3 and the $20 \times 10 \times 20$ mm^3 LSO crystal respectively. From these figures it can be seen that the lower bound increases further away from the APD array and near the edges of the crystal. Therefore, the thickness of the $20 \times 10 \times 10$ mm^3 can not be increased in order to increase the sensitivity without degrading the resolution. This is enhanced by the fact that most interactions occur in the front part of the crystal. For example, in a 20 mm thick LSO crystal approximately 70% of the annihilation photons that interact inside the crystal interact in the first 10 mm. Placing the APD array on the front side of the crystal could help in this respect. Another solution might be the use of double-sided readout, as can be seen in Fig. 4(a), which allows one to increase the crystal size to $20 \times 10 \times 20$ mm^3 without sacrificing position resolution.

The distributions of the Cramér–Rao lower bound on the x, y and z-coordinate in the five detector geometries with polished surfaces clad in Teflon are shown in Fig. 5. When comparing Figs. 5(a) and 5(b), it can be seen that the lower bound is higher in y-direction for all geometries except the $20 \times 20 \times 20$ mm^3 crystal. This is caused by the fact that in these geometries the crystals are twice as long in the x-direction than in the y-direction, while the lower bound is higher near the edges. As can be seen from Fig. 5(c), for the designs that are read out by two APD arrays the lower bound in the z-direction is slightly lower than

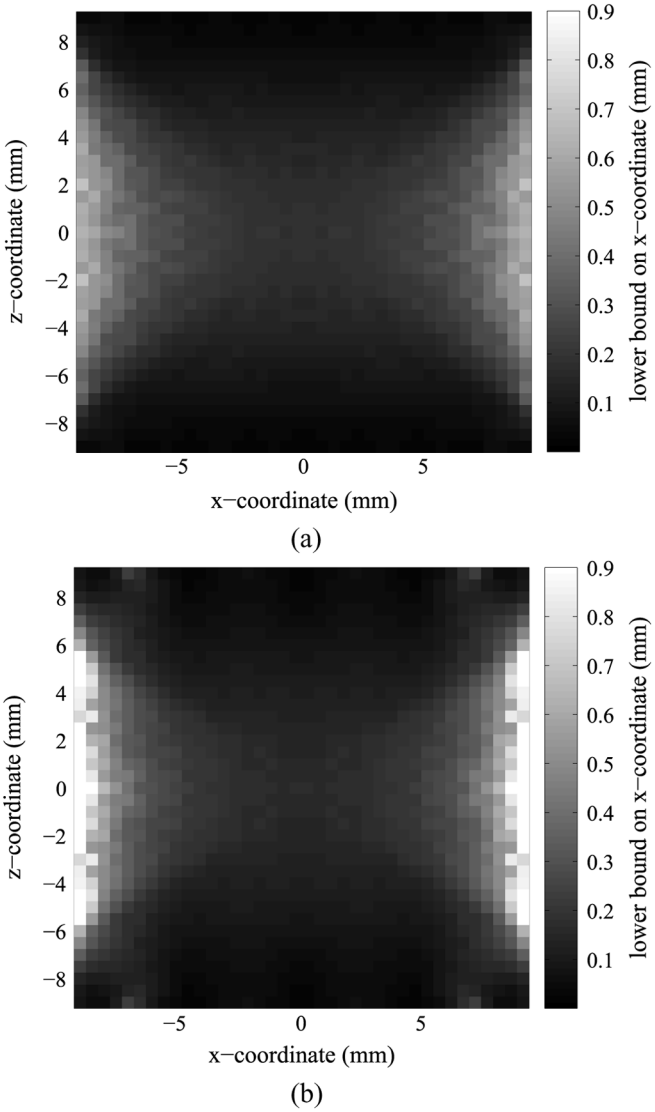

Fig. 4. The lower bound on the x-coordinate as a function of position in the x-z plane in the center of the $20 \times 10 \times 20$ mm^3 LSO crystal clad in Teflon for two pixel sizes: 1.6 mm × 1.6 mm (a) and 3.9 mm × 3.9 mm (b).

in the other two directions. Compared to the other designs, the design read out by only one APD array on the back performs worst in the z-direction. This is probably because the other designs have two APD arrays opposite each other in the z-direction making a better estimation of the z-coordinate possible.

The $20 \times 10 \times 10$ mm^3 and the $20 \times 10 \times 20$ mm^3 crystal perform approximately equally well when looking at the x-coordinate. The same is true for the y-coordinate, but the $20 \times 10 \times 20$ mm^3 crystal performs significantly better when estimating the z-coordinate for the reason mentioned in the preceding paragraph.

Furthermore, the $20 \times 10 \times 20$ mm^3 and the $20 \times 14(10) \times 20$ mm^3 crystal show similar performance. While the tapered crystal has a slightly higher larger bound on the x-coordinate, it has a slightly smaller lower bound on the y-coordinate. Therefore, adding a taper to the crystal hardly influences the resolution, in spite of the fact that the back surface of the tapered crystal is significantly larger

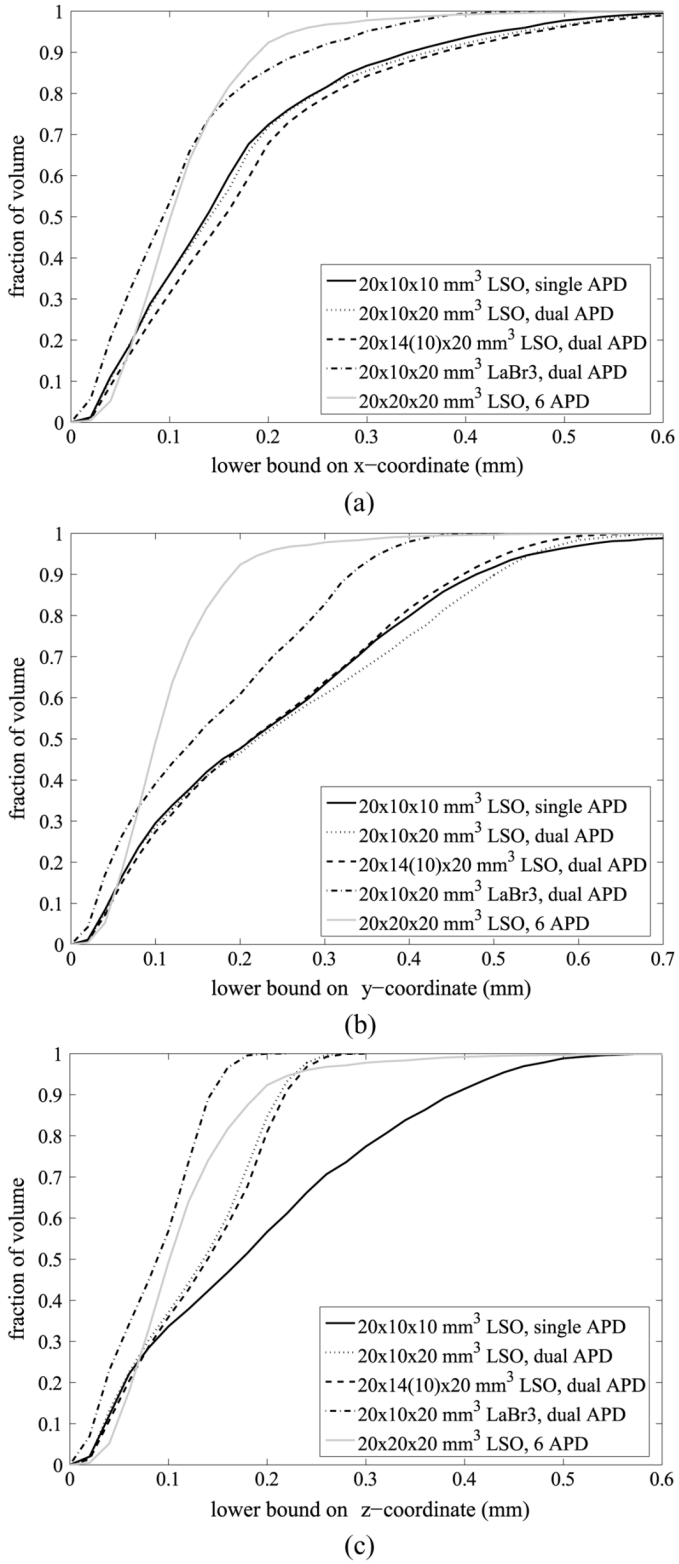

Fig. 5. Cumulative distribution of the Cramér–Rao lower bound on the x, y and z-coordinate for the five detector geometries. The y-axis shows the fraction of the crystal volume for which the lower bound is smaller than the value given on the x-axis.

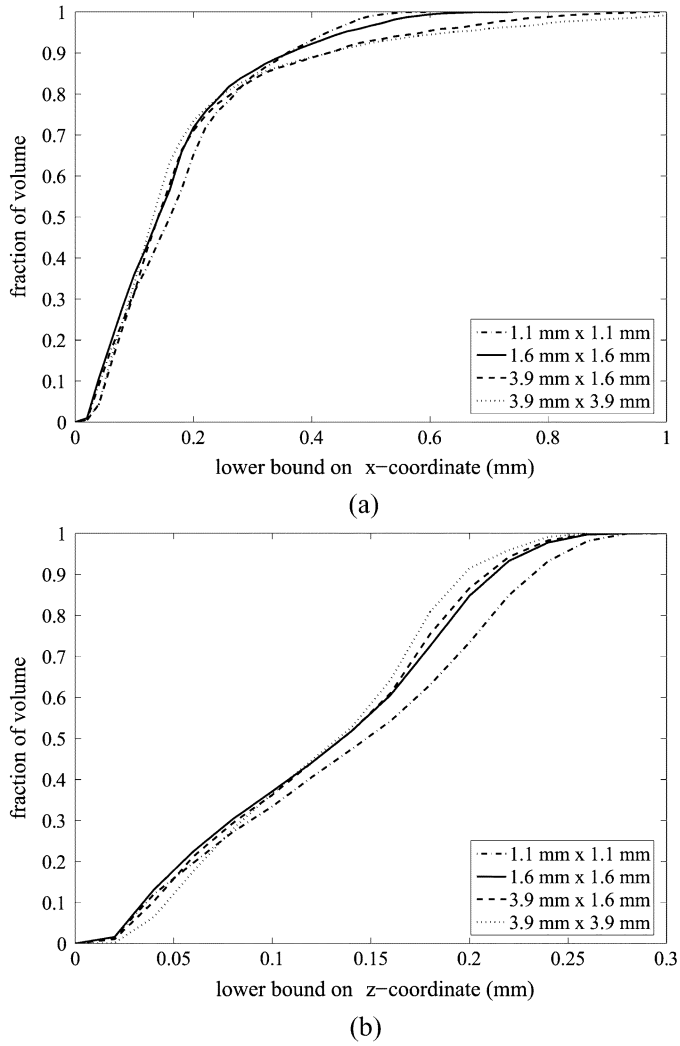

Fig. 6. Cumulative distribution of the Cramér–Rao lower bound on the x-coordinate for various APD pixel sizes. The y-axis shows the fraction of the crystal volume for which the lower bound is smaller than the value given on the x-axis.

than the APD array. This is probably caused by the fact that the part of the crystal that sticks out is very close to the APD array, while the resolution improves closer to the APD array as is shown in Figs. 3 and 4. Another factor could be that there is less internal trapping of light, since the taper reflects light towards the back side of the crystal.

Concerning the $LaBr_3$ crystal, one would expect the lower bound to be approximately a factor $\sqrt{61\,000/26\,000}$ lower (see (6)) than that of the corresponding LSO crystal, because all relevant parameters except the light yield are approximately the same. This is indeed the case. The $20 \times 10 \times 20$ mm^3 $LaBr_3$ crystal and the $20 \times 20 \times 20$ mm^3 LSO crystal read out on all six sides perform approximately equally well for the x-coordinate, but for the y-coordinate the performance of the $LaBr_3$ crystal is less good. Both designs, however, perform better than the other designs based on LSO. Close to the APD arrays, the $LaBr_3$ crystal performs somewhat better than the $20 \times 20 \times 20$ mm^3 crystal, because the small APD pixel size of the 32 pixel array in the $LaBr_3$ design results in a better estimation close to the APD array.

3) APD Pixel Size: Fig. 6 shows the distribution of the lower bound on the x and z-coordinate in the $20 \times 10 \times 20$ mm^3 polished Teflon clad LSO crystal for various APD pixel

sizes. When estimating the x-coordinate the smaller pixel sizes perform better, while the larger pixel sizes perform better when estimating the z-coordinate. This can probably be explained by assuming that the performance for different pixel sizes is a balance between capturing the shape of the light distribution (small pixel sizes) and good statistics (large pixel sizes, resulting in less dead space). When estimating the x-coordinate the shape of the light distribution is important, so smaller pixel sizes perform better. The z-coordinate can largely be determined by the ratio of the amount light detected on the front surface and that detected on the back surface. This ratio is determined more accurately using larger pixel sizes, because large pixels have less dead space between them. For example, the 1.6 mm $\times$ 1.6 mm pixels have 60% dead space, while the 3.9 mm $\times$ 3.9 mm pixels have only 40% dead space.

Since Fig. 6 does not show in which part of the crystal the resolution changes as a result of changing the pixel size, Fig. 4 shows the lower bounds on the x-coordinate in the x-z plane in the center of the crystal for a pixel size of 1.6 mm $\times$ 1.6 mm and for a pixel size of 3.9 mm $\times$ 3.9 mm. In the center of the crystal and near the APD arrays the lower bounds are approximately equal in both cases. The lower bound increases especially near the edges of the crystal if the pixel size is increased. A possible explanation might be that for a point source of optical photons near the edge of the crystal most of the light will be detected by a small number of pixels near the edge. For larger pixels this number will be smaller, making the determination of the position more difficult.

B. Comparison With Beam Simulations

In order to check whether the results for the lower bounds can indeed be used as a meaningful measure of the performance of a detector, a comparison has been made with resolutions obtained from simulations using perfect beams. These simulations mimic the measurements that are currently being performed within our group [6] and Brussels [7], [8], with the difference that in the simulations a beam width of zero is assumed and electronic noise is not modeled. Simulations with a finite beam width show that the differences between the results presented here and the measurements, are mainly due to the difference in beam width.

Because the Cramér–Rao results describe the detector's ability to estimate the coordinates of a point source of light at a given location inside the crystal, and the beam results describe the detector's ability to estimate the entry point of an impinging gamma photon, the absolute values of both types of results cannot be compared directly. Both types of results must, however, show similar trends if the Cramér–Rao results are to be used as a performance measure for optimizing the detector geometry.

Table I shows the resolutions obtained from the beam simulations for the surface finishes investigated. The standard deviations on the FWHM and the FWTM are estimated to be approximately 0.04 mm and 0.06 mm respectively. The results show no significant differences between the different surface finishes. This agrees with the results from Fig. 2, where the differences between the surface finishes were also very small.

The resolutions obtained from the beam simulations for the different crystal geometries are shown in Table II. The results agree quite well with the results obtained for the lower bounds in these crystals: the $20 \times 10 \times 10$ mm^3 LSO crystal performs worst, probably caused by the fact that most interactions occur furthest away from the APD array, the two 20 mm thick LSO crystals with double sided read out perform equally well, and the $LaBr_3$ crystal performs best. According to the results for the Cramér–Rao lower bound presented in the previous section, the $20 \times 20 \times 20$ mm^3 LSO crystal and the $20 \times 10 \times 20$ mm^3 $LaBr_3$ should perform approximately equally well. The FWHM for the $20 \times 20 \times 20$ mm^3 LSO crystal is larger than the FWHM for the $20 \times 10 \times 20$ mm^3 $LaBr_3$ crystal, but the FWTM is smaller.

TABLE I
SIMULATION RESULTS FOR THE SPATIAL RESOLUTION OF THE $20 \times 10 \times 20$ MM^3 LSO CRYSTAL READ OUT ON TWO SIDES BY AN APD ARRAY USING PHOTON BEAMS SCANNED IN THE x-DIRECTION OVER THE CENTER OF THE CRYSTAL

Surface Finish	FWHM (mm)	FWTM (mm)
Polished, Teflon clad	0.64	2.76
Rough, Teflon clad	0.55	2.73
Polished, absorbing clad	0.57	2.76
Rough, absorbing clad	0.56	2.71
Specular reflecting	0.62	2.81

TABLE II
SIMULATION RESULTS FOR THE SPATIAL RESOLUTION OF THE FIVE DIFFERENT DETECTOR GEOMETRIES USING BEAMS SCANNED IN THE x AND y-DIRECTION OVER THE CRYSTAL

Detector geometry	x-direction		y-direction	
	FWHM (mm)	FWTM (mm)	FWHM (mm)	FWTM (mm)
$20\times10\times10$ mm^3 LSO	0.84	3.24	0.90	3.60
$20\times10\times20$ mm^3 LSO	0.64	2.76	0.62	2.98
$20\times14(10)\times20$ mm^3 LSO	0.66	2.82	0.68	2.99
$20\times10\times20$ mm^3 $LaBr_3$	0.48	2.28	0.54	2.66
$20\times20\times20$ mm^3 LSO	0.60	1.90	–	–

V. CONCLUSION

In this paper the use of the Cramér–Rao lower bound has been proposed for investigating the intrinsic spatial resolution performance of PET detector modules. This performance measure makes a better understanding of the influence of different design parameters on the spatial resolution possible. Firstly, because the measure does not depend on the specific algorithm used to estimate the entry points, secondly because the performance of a detector can be investigated as a function of all three coordinates, and finally because the influence of individual parameters can be made explicit. For example, the effect of the number of primary photons and the quantum efficiency of the APD array on the lower bound can be directly seen from (6).

In the derivation of the Cramér–Rao lower bound it is assumed that the ability to estimate the entry point of an impinging annihilation photon is related to the ability to estimate the the position of a point source of optical photons within the block. If the lower bound is to be used as a meaningful performance measure, it should give the same relative ordering of the performance of different designs as obtained from beam simulations. From the results presented in the previous section this does indeed appear to be the case.

In order to illustrate the method, the influence of surface finish, crystal geometry, and pixel size on the performance were investigated. For the sake of simplicity, only the influence of light transport and detection were investigated. From these simulations a few interesting observations can be made. First of all, it appears that the surface finish of the monolithic scintillator crystals has little influence on the intrinsic resolution of the detector. The polished or rough Teflon clad surfaces therefore appear to be a good choice, because the reflective cladding may improve the energy resolution and the timing properties of the detector.

Several observations can be made concerning the crystal geometries. First, it can be concluded that $LaBr_3$ is an interesting material for further study. Its high light yield improves the lower bound by approximately a factor of 1.5, but the quantum efficiency of the APD has not yet been taken into account. This will have an influence, because the quantum efficiency of the Hamamatsu S8550 for the peak wavelength of $LaBr_3$ is smaller than for the peak wavelength of LSO, viz. 50% compared to 70%. Taking these numbers into account, the improvement is reduced to approximately $\sqrt{0.5/0.7} \cdot 1.5 = 1.3$, see (6), which is still substantial. Secondly, increasing the thickness of the $20 \times 10 \times 10$ mm^3 crystal in order to increase the sensitivity, without adding more APD arrays, is not possible without severely degrading the spatial resolution. Thirdly, tapered crystals, which could improve the sensitivity when placed in a ring, perform as well as rectangular blocks. Finally, the $20 \times 20 \times 20$ mm^3 crystal read out on all sides by single APDs seems promising, since it gives a uniform resolution throughout the detector, but the large area of the APDs in this design will probably lead to a significant increase in the electronic noise, because of a larger dark current and increased detector capacitance. Electronic noise will therefore have to be taken into account in the model, before any definite conclusions can be drawn with respect to this design.

From the comparison of the lower bound for the $20 \times 10 \times 20$ mm^3 crystal for the different APD pixel sizes it appears that the smallest pixel sizes perform best regarding the resolution in the x-coordinate, even though the statistics in the number of optical photons detected per pixel will be worse, and the total number of detected optical photons is also smaller because of the increased amount of dead space between the pixels. This result may change when we add electronic noise to our model, because the electronic noise will have more influence if the number of detected photons per channel is less.

The method derived in this paper has one important limitation, which is the fact that the influence of Compton scattering is ignored. This will especially have an influence when different scintillators are compared to each other. However, when geometries with approximately the same dimensions and using the same scintillator material are compared, the influence of Compton scattering will be the same for all geometries. The model used to illustrate the method is still relatively simple and ignores the influence of quantum efficiency and electronic noise. The quantum efficiency is approximately constant for a given combination of APD array and scintillator and is furthermore a constant factor in the lower bound (see (6)). Therefore, when only the quantum efficiency is added to the model, the conclusions concerning the surface finish, single or double sided read out and pixel size will not change for the Hamamatsu S8550 APD array combined with the LSO crystal. However, as the previous discussion showed, adding electronic noise to the model might influence some of the conclusions. We are therefore working on including electronic noise in our models in order to investigate its influence on the performance.

ACKNOWLEDGMENT

The authors would like to thank L. van Vliet and M. Defrise for their helpful advice and discussions, and Prof. U. Pietrzyk for allowing us to do some of our computations on his computer cluster.

This research was performed in collaboration with the Crystal Clear Collaboration, a CERN Technology Transfer Project grouping a number of European universities and government research institutes.

REFERENCES

[1] A. F. Chatziioannou, "Molecular imaging of small animals with dedicated PET tomographs," *Eur. J. Nucl. Med. Mol. Imag.*, vol. 29, no. 1, pp. 98–114, 2002.

[2] L. E. Adam, J. S. Karp, and M. E. Daube-Witherspoon, "Evaluation of performance of the CPET scanner using standardized measurement techniques," in *Proc. 2000 IEEE Nuclear Science Symp. Conf. Rec.* , Lyon, France, vol. 3, pp. 17/46–17/50.

[3] S. Delorme, R. Frei, C. Joseph, J. Loude, and C. Morel, "Use of a neural network to exploit light division in a triangular scintillation crystal," *Nucl. Instrum. Methods Phys. Res. A*, vol. 373, pp. 111–118, 1996.

[4] D. Clément, R. Frei, J. Loude, and C. Morel, "Development of a 3D position sensitive scintillation detector using neural networks," in *Proc. 1998 IEEE Nuclear Science Symp. Conf. Rec.*, Toronto, ON, vol. 3, pp. 1448–1452.

[5] P. P. Antich, N. Malakhov, R. Parkey, N. Slavin, and E. Tsyganov, "3D position readout from thick scintillators," *Nucl. Instrum. Methods Phys. Res. A*, vol. 480, pp. 782–787, 2002.

[6] M. C. Maas, "Experimental characterization of novel small animal PET detector modules based on scintillation crystal blocks read out by APD arrays," in *Proc. 2004 IEEE Nuclear Science Symp. Conf. Rec.*, <AUTHOR: CITY, COUNTRY?>, pp. 2942–2946.

[7] P. Bruyndonckx, S. M. A. Léonard, J. Liu, S. P. K. Tavernier, P. Szupryczynski, and A. Fedorov, "Study of spatial resolution and depth of interaction of APD-based PET detector modules using light sharing schemes," *IEEE Trans. Nucl. Sci.*, vol. 50, no. 5, pp. 1415–1419, Oct. 2003.

[8] P. Bruyndonckx, "Neural network-based position estimators for PET detectors using monolithic LSO blocks," *IEEE Trans. Nucl. Sci.*, vol. 51, no. 5, pp. 2520–2525, Oct. 2004.

[9] A. Stuart and J. K. Ord, *Kendall's Advanced Theory of Statistics Volume 1—Distribution Theory*. London, U.K.: Edward Arnold, 1991.

[10] S. Agostinelli, "GEANT4—A simulation toolkit," *Nucl. Instrum. Methods Phys. Res. A*, vol. 506, no. 3, pp. 250–303, 2003.

[11] C. W. E. van Eijk, "Inorganic scintillators in medical imaging," *Phys. Med. Biol.*, vol. 47, pp. R85–R106, 2002.

[12] J. W. LeBlanc and R. A. Thompson, "A novel PET detector block with three-dimensional hit position encoding," *IEEE Trans. Nucl. Sci.*, vol. 51, no. 3, pp. 746–751, Jun. 2004.

[13] A. Levin and C. Moisan, "A more physical approach to model the surface treatment of scintillation counters and its implementation into DETECT," in *Proc. 1996 IEEE Nuclear Science Symp. Conf. Rec.*, Anaheim, CA, vol. 2, pp. 702–706.

[14] *Geant4 Physics Reference Manual*, Geant4 7.0, Dec. 2004.

[15] C. Moisan, M. S. Andreaco, J. G. Rogers, S. Paquet, and D. Vozza, "Segmented LSO crystals for depth-of-interaction encoding in PET," in *Proc. 1997 IEEE Nuclear Science Symp.*, Albuquerque, NM, vol. 2, pp. 1112–1116.

[16] A. Braem, "Feasibility of a novel design of high resolution parallax-free Compton enhanced PET scanner dedicated to brain research," *Phys. Med. Biol.*, vol. 49, pp. 2547–2562, 2004.